Modeling the Performance of an Integrated Battery and Electrolyzer System

Raventos, Andrea Mangel; Kluivers, Gerard J.; Haverkort, J. W.; De Jong, Wiebren; Mulder, Fokko M.; Kortlever, Ruud

DOI
10.1021/acs.iecr.1c00990

Publication date
2021

Document Version
Final published version

Published in
Industrial and Engineering Chemistry Research

Citation (APA)
Raventos, A. M., Kluivers, G. J., Haverkort, J. W., De Jong, W., Mulder, F. M., & Kortlever, R. (2021). Modeling the Performance of an Integrated Battery and Electrolyzer System. *Industrial and Engineering Chemistry Research*, *60*(30), 10988-10996. https://doi.org/10.1021/acs.iecr.1c00990

I&EC research
Industrial & Engineering Chemistry Research

pubs.acs.org/IECR
Article

Modeling the Performance of an Integrated Battery and Electrolyzer System

Andrea Mangel Raventos, Gerard Kluivers, J.W. Haverkort, Wiebren de Jong, Fokko M. Mulder, and Ruud Kortlever*

Cite This: *Ind. Eng. Chem. Res.* 2021, 60, 10988−10996

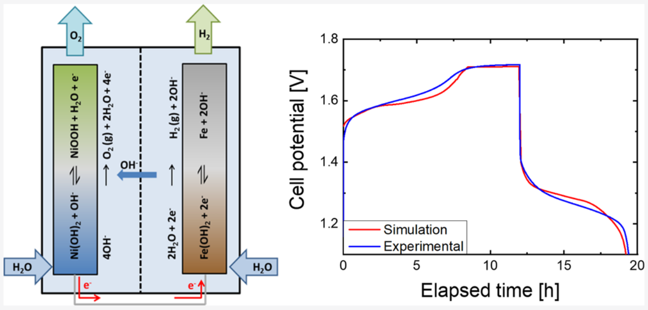

ABSTRACT: Both daily and seasonal fluctuations of renewable power sources will require large-scale energy storage technologies. A recently developed integrated battery and electrolyzer system, called battolyser, fulfills both time-scale requirements. Here, we develop a macroscopic COMSOL Multiphysics model to quantify the energetic efficiency of the battolyser prototype that, for the first time, integrates the functionality of a nickel−iron battery and an alkaline electrolyzer. The current prototype has a rated capacity of 5 Ah, and to develop a larger, enhanced system, it is necessary to characterize the processes occurring within the battolyser and to optimize the individual components of the battolyser. Therefore, there is a need for a model that can provide a fast screening on how the properties of individual components influence the overall energy efficiency of the battolyser prototype. The model is validated using experimental results, and new configurations are compared, and the energy efficiency is optimized for the scale-up of this lab-scale device. Based on the modeling work, we find an optimum electrode thickness for the nickel electrode of 3 and 2.25 mm for the iron electrode with optimal electrode porosities in the range of void fraction of 0.15−0.35. Additionally, electrolyte conductivity and the gap thickness are found to have a small effect on the overall efficiency of the device.

1. INTRODUCTION

The increasing share of wind and solar energy, together with COP21 Paris targets set for renewable energy capacity growth, implies an increase in the variability of future electricity generation.[1,2] Therefore, an electrical grid completely based on largely intermittent renewable energy sources will require widespread and efficient energy storage.[3,4] Currently, fossil fuels provide the buffer capacity necessary to balance this mismatch between energy supply and demand.[1,5] As the capacity of renewable energy increases and fossil fuel use decreases, energy storage technologies will be key for developing grids with higher flexibility and the large-scale utilization of renewable energy sources.[6,7]

Batteries are a good option to cover short-term grid fluctuations because of their dynamics and high round-trip efficiency, typically around 80%.[8,9] However, because of their cost, limited cycling rate, self-discharge, and low specific energy storage capacity (energy stored per unit mass), large-scale, longer-term storage options are required alongside battery capacity.[7,8] An alternative solution for long-term energy storage is the production of fuels using renewable energy. Hydrogen is an example of such a fuel that can either be burned in a gas-fired internal combustion engine and gas turbine or electrochemically converted in a fuel cell to generate electricity. The advantages of using hydrogen as an energy carrier include it being a carbon-free fuel with a high mass specific energy density.[8,10,11] In addition to being a fuel, hydrogen is also used as feedstock in the chemical industry, as well as in the refining industry, food industry, metallurgical industry, and electronics industry.[12]

An integrated battery and electrolyzer device, known as the battolyser, has recently been developed.[6] The battolyser was demonstrated as a possible energy storage solution, as its battery functionality can stabilize short-term electricity fluctuations while its electrolyzer functionality can stabilize long-term seasonal fluctuations.[6,13] Furthermore, the device was shown to be stable for more than 300 cycles.[13] As can be seen in Figure 1, the battolyser utilizes two different energy storage functionalities: a nickel−iron battery and an alkaline electrolyzer. The nickel−iron battery, also known as the Edison battery, serves as a short-term energy storage mechanism.[14] Electricity can be stored and generated from the materials in the electrodes via the $Ni(OH)_2/NiOOH$ and $Fe(OH)_2/Fe$

Received: March 12, 2021
Revised: June 30, 2021
Accepted: July 2, 2021
Published: July 15, 2021

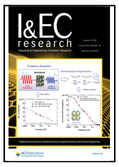

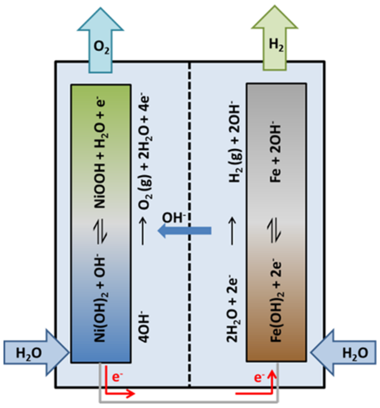

Figure 1. Schematic illustration of the chemical reactions that occur during charging, overcharging, and discharging of the battolyser.

redox couples.[15] When the maximum battery capacity is reached, the battolyser makes use of the electrocatalytic properties of Fe and NiOOH for electrochemical hydrogen and oxygen evolution, and the device then acts as an alkaline electrolyzer. Thereby, the excess electricity that cannot be stored in the battery functionality is used to split water molecules from the electrolyte, generating hydrogen and oxygen.[14,15]

Because the system operates as both a battery and an electrolyzer, the capacity limit of this system is not fixed by the amount of the active battery material. An additional advantage of using Ni−Fe batteries in the system is that they are very robust and have a life time of approximately 3000 cycles or 20 years.[13,16] The total energy efficiency of the system, combining battery functionality and hydrogen production, is around 90%.[13] Moreover, the device can follow electricity fluctuations typical of renewable energies, such as solar and wind.[13]

Here, we report on the development of a macroscopic model that can quantify the energy efficiency of the existing battolyser prototype. The current battolyser prototype has a rated capacity of 5 Ah, and to develop a larger, more optimized system, it is necessary to characterize the processes occurring within the battolyser and to optimize the individual components of the battolyser. Therefore, there is a need for a model that can provide a fast screening on how the properties of individual components influence the overall energy efficiency of the battolyser prototype.

Many empirical and semiempirical models have been proposed to simulate alkaline electrolysis;[17,18] however, our approach integrates thermodynamics, kinetics, and transport mechanisms to model the performance of the integrated storage device including details of the specific geometry. Furthermore, only a handful models of alkaline electrolysis have been validated experimentally.[19] Many models simulate the *I*−*V* characteristics of different electrochemical cells, but not many can determine the effect of the geometric cell parameters on the functionality.[17,19,20] The model developed here is validated using experimental results, and new configurations and design parameters have been compared and optimized for the upscaling of this lab-scale device. The model developed is able to predict the energy efficiency of different configurations without having to test these configurations individually, which is of utmost importance in upscaling the current battolyser prototype. In addition, the developed model is to the best of our knowledge the first model that integrates a battery and electrolyzer functionality for nickel−iron batteries. A comprehensive model for zinc−nickel batteries has been recently published.[21] Using the model, we will give design recommendations that can improve the device efficiency, taking into account both the battery and electrolyzer functionalities and the trade-offs inherent for the optimization. Some of the limitations of the current model include bubble production and thermal effects, and future efforts can be made to study these effects.

2. MODELING AND EXPERIMENTAL METHODS

2.1. Model. A one-dimensional (1D) COMSOL Multiphysics model has been developed to simulate the integration of battery and electrolyzer functionalities of the battolyser system. The COMSOL Multiphysics model is a time-dependent partial differential equation system using a backward differentiation formula (BDF) solver with variable size up to extremely fine finite elements. This tool was chosen to solve the governing physical equations detailed here. To describe the integration of both storage functionalities, a number of aspects must be taken into account, including

- the diffusion of hydroxide ions from one electrode to another and the concentration profiles of hydroxide and potassium ions through the width of the cell,
- the calculation of the cell potential, including the overpotential of each chemical reaction,
- the electrochemical reactions for the battery functionality including the nickel positive electrode and the iron negative electrode reactions and the determination of the state of charge of the battery,
- the electrochemical reactions for the electrolyzer functionality including the hydrogen evolution reaction (HER) and oxygen evolution reaction (OER), and
- the bubble production.

These phenomena are all quantified for different time scales, therefore a time-dependent model that simulates both battery and electrolyzer functionalities in the *x* dimension of the battolyser cell is built.

The COMSOL Multiphysics model is a time-dependent partial differential equation system using a BDF solver with variable size extremely fine finite elements. A schematic representation of the electrochemical cell is presented in Figure 2. The cell is composed of an iron negative electrode, a nickel positive electrode (both from Ironcore), and a polyphenylene sulfide fabric commercial separator (Zirfon PERL, AGFA). All three components are porous and

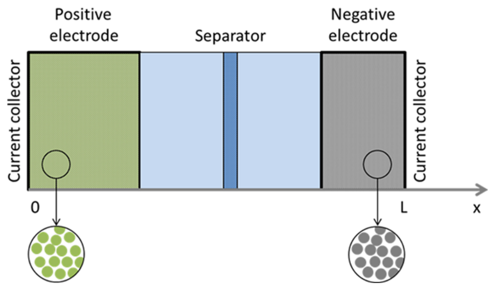

Figure 2. Schematic diagram of battolyser cells and their model representation including the $Ni(OH)_2$ positive electrode, aqueous KOH electrolyte, polyphenylene sulfide separator, and $Fe(OH)_2$ negative electrode.

https://doi.org/10.1021/acs.iecr.1c00990
Ind. Eng. Chem. Res. 2021, 60, 10988−10996

considered to be filled with aqueous liquid 5 M KOH electrolyte. A cross section of the battolyser is modeled in one dimension. Thereby, length and height effects are neglected. The average particle diameter is considered for solid diffusion. The model includes effects of the electronic current conduction in the electrodes and ionic charge transport through the electrodes, electrolyte, and separator.

This model simulates mass transport in the electrolyte and within the particles that form the electrodes. A similar model was developed by Newman and Paxton to describe NiMH batteries. A similar approach is taken, but secondary reactions are included to take into account HER/OER production. The reaction source term includes Butler−Volmer kinetics, both for the charging/discharging reactions and the gas production reactions. All the simulations are considered at ambient temperature and pressure. Thermal effects are not considered as the current density is relatively low compared to industrial electrolyzer systems. Therefore, thermal effects due to high current density effects are assumed to be negligible. Pressure effects are not considered as the system operates under atmospheric pressure conditions.

2.1.1. Diffusion and Migration. The transport of species in the electrolyte is calculated using the Nernst−Planck equation:

$$N_i = -D_i \nabla c_i - z_i u_{\mathrm{m}i} F c_i \nabla \phi_{\mathrm{l}} \tag{1}$$

where N_i is the particle flux of species i, D_i is the diffusion coefficient, c_i is the concentration, z_i is the valence, $u_{\mathrm{m}i}$ is the mobility, and F is Faraday's constant.

Because there is no forced flow, transport is due to diffusion and migration. An effective ambipolar diffusivity is used for the electrolyte, which considers the diffusion of both ions in the electrolyte. The diffusive flow of K^+ and OH^- is coupled because of the requirement of electroneutrality on the movement of the respective ions.

As the electrolyte used is highly concentrated (5−6.5 M KOH), a concentrated solution model is considered, and therefore, changes in conductivity and diffusivity in the electrolyte are concentration-dependent. The electrolyte is modeled using concentrated solution theory with three mobile species: K^+, OH^-, and H_2O. Concentrated electrolyte theory for a binary (1:1) electrolyte is used to describe charge transport in the electrolyte phase. For a binary electrolyte with equal valences, electroneutrality stipulates that the concentrations of OH^- and K^+ are taken to be equal at all points in space.

The effective ionic conductivity and electronic conductivity are corrected to factor in the tortuosity of a porous electrode material filled with a liquid electrolyte using the following expression:

$$\sigma_{\mathrm{s}}^{\mathrm{eff}} = \sigma_{\mathrm{s}} \varepsilon_{\mathrm{s}}^{\gamma} \tag{2}$$

where $\sigma_{\mathrm{s}}^{\mathrm{eff}}$ is the effective conductivity of the solid electrodes and γ is the Bruggeman coefficient set to 1.5 for a packed bed of spherical particles.[22] The diffusion coefficient for the electrolyte is corrected to take into account tortuosity and porosity in the same way.

Diffusivity in the electrolyte gap is faster because of bubble movement. The empiric relationship used to describe the effect of bubbles in the electrolyte gap is further discussed in a separate section.

2.1.2. Potential. The electronic current in the solid electrode particles is determined by Ohm's law:

$$i_{\mathrm{s}} = -\sigma_{\mathrm{s}} \nabla \phi_{\mathrm{s}} \tag{3}$$

where i_{s} is the electronic current, σ_{s} is the solid conductivity, and ϕ_{s} is the potential difference in the solid. The ionic current through the liquid electrolyte can be described by:

$$i_{\mathrm{l}} = -\sigma_{\mathrm{l}} \nabla \phi_{\mathrm{l}} - \frac{2\sigma_{\mathrm{l}} RT}{F}\left(1 + \frac{\partial \ln a}{\partial \ln c_{\mathrm{l}}}\right) \cdot \left(t_{+} + \frac{c_{\mathrm{l}}}{c_0}\right) \nabla \ln c_{\mathrm{l}} \tag{4}$$

where i_{l} is the ionic current through the electrolyte, σ_{l} is the conductivity of the liquid electrolyte, ϕ_{l} is potential in the electrolyte, c_{l} is the concentration of hydroxide ions in the electrolyte, c_0 is the initial concentration of hydroxide ions, a is the activity, R is the universal gas constant, T is temperature, and F is Faraday's constant. The total current is:

$$i = i_{\mathrm{l}} + i_{\mathrm{s}} \tag{5}$$

where is i_{s} the electronic current through the solid electrodes and i_{l} is the ionic current through the electrolyte.

The boundary condition at the grounded electrode is:

$$\phi_{\mathrm{s}} = 0 \tag{6}$$

The nickel electrode's external metal surface is at one potential, depending on the applied constant current. This defines whether the battery is charging or discharging by multiplying the current value with a step function, which changes from 1 to −1 depending on the time. The iron electrode is also at a constant potential, equal to zero because it is considered to be grounded.

The overpotential is calculated as the difference between the electrode potential, the electrolyte potential, and the standard electrode potential.

$$\eta = \phi_{\mathrm{s}} - \phi_{\mathrm{l}} - E^0 \tag{7}$$

where η is the overpotential and E^0 is the standard electrode potential of the electrode material. The equilibrium potential of the positive electrode is composition-dependent and based on experimental data.[22] A more accurate description of the dependence of the equilibrium potential on the state of charge of the electrode can be found in the Supporting Information, Figure S1. Ohm's law is used to describe charge transport in the electrodes. Diffusion inside the porous electrodes is modeled by Fickian diffusion, assuming that the particles are spherical.

Both electrodes are modeled as consisting of spherical porous particles with uniform size and porosity. Particle size and porosity are assumed to be independent of the state of charge of the battery and constant. Each electrode is considered as a two-phase system consisting of a porous particle matrix and a liquid electrolyte. Gaseous products are modeled as dissolved species in the liquid electrolyte. Gas build-up is therefore not considered in the model, only dissolved hydrogen and oxygen in the liquid electrolyte, which is a reasonable assumption for low current density operation. Bubbles are considered to increase the ambipolar diffusivity coefficient of the electrolyte. The reverse reactions for both the HER and OER are not considered.

2.1.3. Electrochemical Reactions. The following electrochemical reactions describe the Faradaic processes occurring at the electrodes.

On the positive nickel electrode:

$$\mathrm{Ni(OH)_2 + OH^- \leftrightarrow NiOOH + H_2O + e^-}$$

$$4\,OH^- \rightarrow O_2 + 2\,H_2O + 4\,e^-$$

On the negative iron electrode:

$$Fe(OH)_2 + 2\,e^- \leftrightarrow Fe + 2\,OH^-$$

$$2\,H_2O + 2\,e^- \rightarrow H_2 + 2\,OH^-$$

During charging, hydroxide ions move from the negative electrode to the positive electrode. As the battery starts charging, the catalysts for oxygen evolution and hydrogen evolution are generated, resulting in oxygen production on the nickel oxyhydroxide (NiOOH) particles and hydrogen production on the metallic iron surface. The cell potential increases during charging, dependent on the state of charge of the battery. Once fully charged, the device performs solely as an alkaline electrolyzer.

Chemical reaction rates are derived from the general Butler–Volmer equation:

$$j = j_0 \cdot (e^{\alpha_a F\eta/RT} - e^{-\alpha_c F\eta/RT}) \tag{8}$$

where j is the current density, j_0 is the exchange current density, α_a is the anodic charge transfer coefficient, α_c is the cathodic charge transfer coefficient, η is the overpotential, F is Faraday's constant, R is the universal gas constant, and T is the temperature.

The model considers transport of species in one direction. The material balance for species i is given by:

$$R_i = \frac{\partial c_i}{\partial t} + \nabla \cdot (-D_i \nabla c_i - z_i u_{mi} F c_i \nabla \phi_l) \tag{9}$$

where R_i is the reaction rate, c_i is the concentration of species, D_i is the diffusion coefficient, z_i is the number of electrons, u_{mi} is the mobility, and ϕ_l is the ionic potential in the liquid electrolyte.

Chemical reactions are proportional to the electrochemically active surface area. This is measured from the active material via Brunauer–Emmett–Teller (BET) measurements and can be found in the Supporting Information, Section D.

The intercalation reaction is taken into account as a solid concentration, which can then be used to calculate the state of charge considering the amount of active material available:

$$\mathrm{SoC} = \frac{c_s}{c_{s,max}} \tag{10}$$

where c_s is the average concentration of the reacted species in the electrode materials and $c_{s,\,max}$ is the maximum concentration that can be loaded, which indicates the theoretical capacity of the battery materials. The exchange current density of the secondary reactions, HER and OER, is assumed to increase linearly with the local state of charge (SoC) of the electrodes. This assumption is made to simulate the different catalytic activity of the discharged and charged battery electrode materials. The gaseous products of the electrochemical reactions are assumed to remain in the liquid phase. In reality, because of the low solubility of both O_2 and H_2, only a small fraction of the gaseous products will dissolve in the electrolyte while most will bubble out. The products of charging and discharging electrochemical reactions remain in the solid phase.

2.1.4. Bubble Effects. Although the gas fraction is not explicitly calculated, the increased mass transfer due to bubble movements is simulated as a simple empirical relation. The effects of bubble break-off and the movement of fluid that replaces that space are calculated using the Rousar correlation in a characteristic Sherwood number, Sh_1:[23,24]

$$Sh_1 = \sqrt{\frac{12}{\pi}} Re_G^{0.5} Sc^{0.5} \Theta^{0.5} \tag{11}$$

For the effect of growth and wake flow, Vogt's correlation for low bubble coverage (Θ smaller than 0.5) is used to calculate another characteristic Sherwood number, Sh_2:[24]

$$Sh_2 = \frac{2}{\sqrt{5}} Re_G^{0.5} Sc^{0.34} \left(1 - \frac{\sqrt{8}}{3} \frac{R_a}{R} \Theta^{0.5}\right)(1 + \Theta) \tag{12}$$

where the total effect of the bubbles is calculated as:

$$Sh_{bubbles} = (Sh_1^2 + Sh_2^2 + 1)^{0.5} \tag{13}$$

The bubble coverage, Θ, is calculated using the empirical relationship developed by Vogt on a flat-plated electrode:[23]

$$\Theta = 0.023 \left(\frac{I}{A}\right)^{0.3} \tag{14}$$

where I is the current and A is the geometric area.

The Reynolds and Schmidt numbers are described as:

$$Re_G = \frac{V_{gas}}{A} \frac{d_b}{\nu} \tag{15}$$

$$Sc = \frac{\nu}{D} \tag{16}$$

where d_b is the characteristic length scale, ν is the kinematic viscosity of the electrolyte, and D is diffusivity, and the gas volume flux can be defined as:

$$\frac{V_{gas}}{A} = \frac{j}{zF} \frac{RT}{P} \tag{17}$$

where R, T, F, and P are known, j is the gas evolving current density, and z is the number of electrons.

Simplifications from Vogt et al.[23] and Burdyny et al.[24] are used to calculate the effect of bubbles on the diffusion coefficient of the electrolyte. Assumptions of this simplification evaluate the gas production on a flat-plane electrode. As the pocket-type electrodes used in the battolyser are porous, the active surface area per volume will be larger; consequently, the electrochemical gas production will be higher. Following Vogt's assumptions, R_a/R is assumed to be 0.75. The resulting value is used to enhance the diffusion coefficient during charging, increasing the ambipolar diffusivity by a factor of 30%.

2.2. Experimental Validation. An experimental setup was designed to validate the model results. The setup consists of a commercial Ni–Fe battery (Ironcore Batteries, 10 Ah capacity) in its original casing. A schematic representation of the cell design, the commercial batteries, and the composition of the electrode materials can be found in the Supporting Information. The electrodes are kept separate by rubber separator plates to avoid a short-circuit. The setup includes three nickel electrodes and two iron electrodes. The battery setup was conditioned as recommended by the manufacturer. The conditioning procedure consisted of 15 cycles of charge/discharge at C/5 rate. During these cycles, ultrapure water is added to replenish the electrolyte once a week.

The electrolyte used in the validation experiments is a 5 M KOH solution. Details on the conductivity of KOH are presented in the Supporting Information, Figure S10. A 5 M KOH electrolyte is chosen because of its high conductivity, whereas further increasing the KOH concentration did not significantly increase the conductivity. Ultrapure water, from a Milli-Q water purification system, and KOH flakes (85%, Merck) were used to prepare the electrolyte.

The electrodes used in the experimental tests are commercial electrodes purchased from Iron Core Power, taken from commercial nickel−iron batteries with a nominal capacity of 10 Ah. The positive nickel electrode is prepared from $Ni(OH)_2$ precipitated from a nickel sulfate solution using NaOH. This is then filtered, washed, and dried. The resulting hydroxide is ball-milled with a 13 wt % graphitic carbon additive to increase the conductivity. This material is then compacted and placed in nickel-coated steel perforated pockets. The negative iron electrode is composed of ground magnetite Fe_3O_4, metallic iron, and 2 wt % graphitic carbon. NaCl is added as a pore former. After compacting and sintering at 700 °C, the NaCl is dissolved. The active material is compacted and collected in nickel-coated steel perforated pockets.

The particle size distribution of both porous electrode materials was measured via scanning electron microscopy (SEM) images. SEM imaging and energy-dispersive X-ray spectroscopy were performed using a JEOL JSM 6500F electron microscope. The measured average particle size is used to model diffusion inside the electrode particles. More information can be found in Section B of the Supporting Information.

The electrochemically active surface area (ECSA) was measured experimentally using the BET technique. A Gemini VII 2390p analyzer was used to perform this measurement. It is assumed that the porosity of the materials is independent of state of charge and therefore does not change throughout the charge/discharge cycles.

The cell was charged at a constant current of 2 A for a duration of 12 h to account for the total capacity and an additional 2 h of gas production. Subsequently, the cell was discharged at a constant current of −2 A or until the cell potential dropped to 1.1 V. This is done to limit the iron reaction to the first discharge plateau.

3. RESULTS AND DISCUSSION

3.1. Model Validation.

To validate the COMSOL Multiphysics model, a representation of the commercial cells is developed. The geometry of the validation model is presented in Figure 3a. Using this 1D cell geometry simulation, the model is validated experimentally. Experimental and modeling results of the variation of cell potential during charge/discharge cycles at constant current and the gas production quantities are compared. A 1D approach is chosen because it is found to show good agreement with experimental data and, as bubble formation is not included in the model, height differences will not be taken into account. Therefore, a 1D version that agrees with the experimental data is used to optimize the setup.

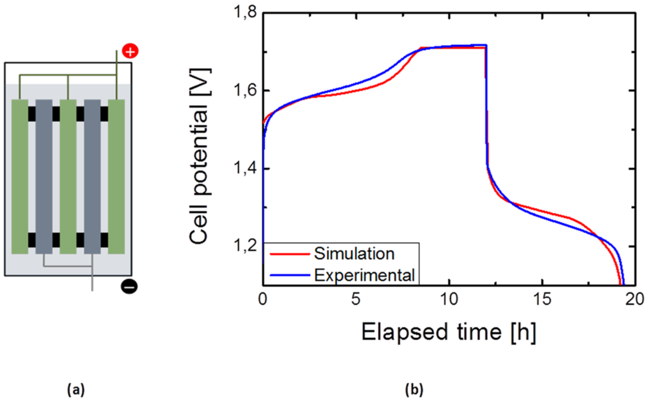

(a) (b)

Figure 3. (a) Schematic diagram of the cell geometry used for validation and (b) comparison of the cell potential during charge and discharge cycles at constant current for experimental and simulation results. Cell potential vs time during a galvanostatic charge and discharge cycle. Charging and discharging at C/5 rate equal to 2 A.

As shown in Figure 3b, the simulated onset potentials of the battery charging reactions and the gas production reactions are very similar to the experimental values. The total discharge capacity is also predicted very accurately. The transition from battery charging in the first hours of operation to gas production, the plateau observed between 9 and 12 h of operation, is smoother in the experimental results than in the modeling results. A possible explanation for this difference is the use of a linear relationship between the exchange current density of the HER and the SoC of the battery electrodes. Because the catalyst for the HER is produced during charging, gas production will be dependent on the overall SoC of the battery. As can be seen in Figure S6, gas production can be described as two separate linear relationships with different slopes; however, in the model this is simplified to a single linear relationship. The simplification of the dependence of gas production with SoC could therefore explain the smoother transition in experimental data. Particle size and porosity are assumed to be independent of the SoC, and this assumption could also be a possible explanation for the discrepancies between the simulation and the experimental results.

The total gas production quantities predicted by the model were validated with small-scale experimental measurements of the volumes of H_2 and O_2 produced during operation. More information on the measurement of O_2 and H_2 production can be found in section F of the Supporting Information. At the end of the charging time, after 12 h of applying current to the system, the total hydrogen production predicted by the model is 0.2 mol. Experimentally, we measured gas production for 9.5 h. With this data, we extrapolated the total gas production for the total 12 h simulated. Using this linear extrapolation, we obtain a production of 5 L of gas in 12 h of total charging time, and using the pressure and temperature of the lab at the moment, together with GC measurements of the percentage of hydrogen present in the sample, we measured hydrogen production to be 0.194 mol. This is in accordance with the amount of hydrogen predicted, therefore the model in this respect corresponds with experimental measurements.

Further validation is done by performing galvanostatic charge and discharge cycles at different current rates. The validation data at different currents are presented in section G of the Supporting Information. Important parameters such as the potential for gas evolution and the battery capacity are modeled correctly in accordance with the experimental data. The slight differences between experimental and modeling results can be explained by the simplifications and assumptions used to build the model, as described above, and are small enough to proceed with using the built model for the subsequent optimization of the unit cell.

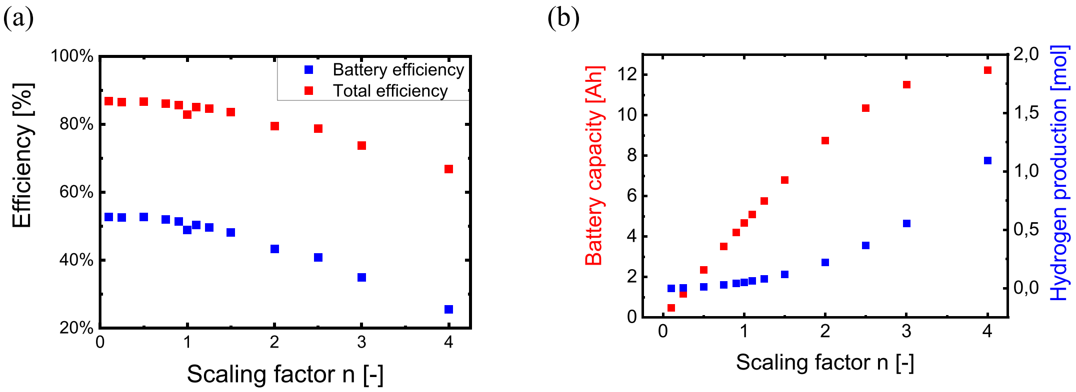

Figure 4. (a) Battery and total integrated energy efficiency with respect to the scaling electrode thickness factor, where *n* is multiplied by the electrode thickness to analyze the effect of decreasing and increasing the electrode thickness, and (b) battery capacity and total hydrogen production vs scaling electrode thickness factor.

3.2. Optimization of Battolyser Parameters. The main objective of this study is to optimize cell parameters to increase the energetic efficiency of the battolyser. The energetic efficiency of the battery component can be calculated using eq 18, while the total efficiency of the battolyser considering hydrogen production is calculated using eq 19.

$$\eta_{\text{battery}} = \frac{I_{\text{discharge}} \cdot \int_{t_{\text{discharge}}}^{t_{\text{total}}} V_{\text{cell}}\ \mathrm{d}t}{I_{\text{charge}} \cdot \int_{0}^{t_{\text{discharge}}} V_{\text{cell}}\ \mathrm{d}t} \tag{18}$$

$$\eta_{\text{total}} = \frac{\left(I_{\text{discharge}} \cdot \int_{t_{\text{discharge}}}^{t_{\text{total}}} V_{\text{cell}}\ \mathrm{d}t\right) + (\text{mol H}_2 \cdot \text{HHV})}{I_{\text{charge}} \cdot \int_{0}^{t_{\text{discharge}}} V_{\text{cell}}\ \mathrm{d}t} \tag{19}$$

Using the model parameters validated in the previous section, a two-electrode geometry was simulated using COMSOL Multiphysics software. This setup allows for the efficient separation of hydrogen and oxygen gas produced in the electrolysis functionality of the device by including an open-mesh polyphenylene sulfide fabric separator coated with a mixture of a polymer and zirconium oxide, between the negative and positive electrodes. Zirfon PERL is used industrially in alkaline electrolysis as it is one of the few stable separators at high pH values.[25] Therefore, this configuration is used to optimize the unit cell. The parameters that are modified and optimized are the electrode thickness, electrode porosity, the electrolyte conductivity, and gap thickness.

3.2.1. Electrode Thickness. By modifying the electrode thickness it is possible to modify the energy density of the device as this increases the total amount of active material in a single unit cell. Electrode thickness is varied by multiplying the electrode thickness, maximum theoretical capacity, and current by a certain factor. To keep the charging and discharging time scales constant, the current scales with the amount of active battery material, keeping the current density per active material constant throughout the different scenarios. However, by making the electrode thickness larger, the innermost active material in the porous electrode might be more difficult to charge. Moreover, the distance from one current collector to the other increases as the electrode thickness increases, increasing the ohmic drop in the electrodes. This will cause a decrease in the percentage of the electrode that is effectively used during charging and discharging.

The electrode thickness is multiplied by a scaling factor "*n*" ranging from 0.1 to 4. Results of the efficiencies, battery capacity, and hydrogen production for different electrode thicknesses are presented in Figure 4. Increasing the electrode thickness results in a decreased efficiency as can be seen in Figure 4a. This can be explained by the relatively low electronic conductivity of the electrode materials,[22] which is comparable in order of magnitude to the effective ionic conductivity of the electrolyte. However, this effect has to be balanced with the total battery capacity and the final use the battery will have. Because this device integrates two functionalities, it is possible to optimize for increased battery storage or hydrogen production. For example, if hydrogen production is preferred, thinner electrodes with a very high surface area are more beneficial. If a specific application requires a specific battery capacity, this can be achieved by modifying the electrode thickness to adapt to the discharging capacity and time scale. It is therefore important to compare the practical utilization of the battery electrodes and the charging cycle duration. Furthermore, increasing electrode thickness will decrease the relative cost per active separator area.[26,27]

Figure 4b shows the effect of changing the electrode thickness on the battery capacity and total hydrogen production. Hydrogen production increases more than linear with *n*, resulting in larger increases at larger scaling factors. This can be due to less current being used to charge the battery, as the battery capacity no longer increases linearly with an increasing scaling factor after the thickness is doubled. Because of this, the relationship between battery capacity and hydrogen production changes, resulting in a reduction in both the battery and the total efficiency. Battery capacity begins to plateau after $n = 4$.

By reducing the thickness of the electrodes, there is hardly any change in the efficiency of the device. Nevertheless, it is important to take into account that the battery capacity is reduced because the amount of active material is reduced. Overall, a thinner electrode will result in a higher efficiency because of smaller ohmic drops inside the electrodes. According to Haverkort,[28] thinner electrodes result in higher efficiency. However, this does not take into account the time scales required for charging and discharging. Depending on the intended function of the battery and the resulting time scales

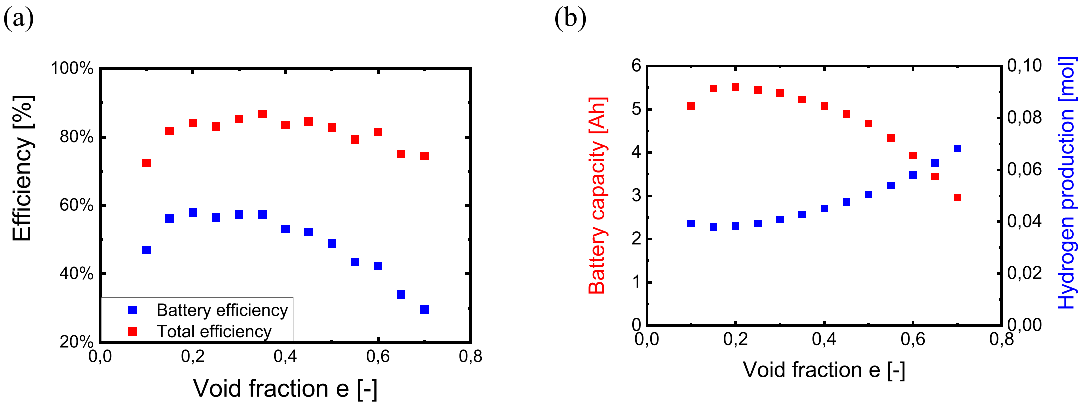

Figure 5. (a) Battery and total integrated efficiency with respect to the electrode porosity, and (b) battery capacity and total hydrogen production vs the electrode porosity.

necessary for charge and discharge of the specific application, battery capacity and discharge time should be included in the analysis.

Taking into account the required battery storage capacity, a thicker electrode is more favorable. Therefore, to increase battery capacity and optimize the energy efficiency of the device, a slightly thinner electrode is chosen as the optimum. Taking into account the time frame or renewable energy availability, this is chosen to keep the capacity of battery storage to hydrogen production relatively equal. This can be modified depending on the application required and should be further optimized taking this into account.

Because of the battery capacity required and the hydrogen production increase related to the increase of the electrode thickness, the value chosen for these electrodes is $n = 0.75$ of the benchmark electrode thickness, corresponding to a nickel electrode thickness of 3 mm and an iron electrode thickness of 2.25 mm. Using these electrode thicknesses results in a battery capacity of 3.5 Ah, with a total energy efficiency of 86%.

3.2.2. Electrode Porosity. Electrode porosity is defined as the electrolyte volume fraction or the percentage of volume taken up by electrolyte. The starting point is $e = 0.5$, meaning that equal volumetric portions of the electrode are taken up by the active material as the electrolyte. This parameter is modified from 0.1 to 0.7, as can be seen in Figure 5.

Decreasing the porosity values results in a lower ionic conductivity in the electrode, as the ionic pathways through the porous electrode material would be limited in an electrode with a low volumetric fraction of the electrolyte.

Because of the high porosity of the electrode material, the void fraction filled with an electrolyte can be larger than the expected void fraction of a packed bed of spheres. Decreasing the porosity results in a higher battery capacity because of the increase in the active material. As can be seen in Figure 5b, as the void fraction increases, battery capacity decreases, as expected. Hydrogen production remains relatively constant with respect to the void fraction.

In the porosity range of 0.15−0.35 electrode volume fraction, an optimum device efficiency is found, as this electrode porosity results in an increased total efficiency. This is comparable to a theoretical optimum for a porous foam-like electrode.[28] Above $e = 0.35$, the battery capacity reduces because less active material can be charged, and more charge is converted to hydrogen. Smaller void fractions result in similar battery capacity but lower overall efficiency.

3.2.3. Electrolyte Conductivity and Gap Thickness. Both the electrolyte conductivity and gap thickness were also optimized, but as expected, at low current densities, the impact on the efficiency is small. Results of this optimization can be found in Figures S8 and S9 in the Supporting Information. In short, the highest conductivity of KOH is chosen as optimal, and for this, a KOH concentration of 5 M is chosen, as a further increase in KOH concentration results only in a small increase in conductivity.[29] Increasing the gap thickness leads to increasing ohmic resistances. Therefore, the smaller the gap between the electrodes, the lower the ohmic drop. However, there is also an accumulation of gaseous products in the gap that results in a reduction of hydroxide concentration close to the electrode surface.[8] Given the simplification of bubble transport in the model, the optimization results do not consider the products bubbling out. Consequently, a constant gap thickness of 3 mm on each side of the membrane was chosen for the sake of comparison.

3.3. Design Recommendations.

Following the energy efficiency-based modeling optimization, the optimal battolyser unit cell will consist of a nickel electrode of 3 mm thickness and an iron electrode of 2.25 mm thick. The electrode material porosity for both electrodes should be designed to be at a void fraction of range between 0.15 and 0.35. This is possible because of the highly porous active electrode material. The electrolyte consists of a 5 M KOH solution, and the electrodes should be placed 3 mm from the membrane, resulting in a total gap thickness of 6.05 mm, including the membrane thickness.

Using the model, specific parameters can be fine-tuned without extensive experimental measurements. This provides a pathway to developing integrated solutions to couple long-term and short-term energy storage. By analyzing the effect of specific parameters and their effect on both battery capacity and total energy efficiency, the unit cell can be optimized to fit a specific application where a certain battery capacity or hydrogen production is required. Furthermore, the model developed can be used as a complex integration tool where specific functionalities can be improved. The integration of a battery and electrolyzer in a single device presents its challenges, as optimizing the device can result in an improvement of only one of the functionalities. Hence, according to the final application of the device, a specific end target can be used as the optimization criteria.

A summary of the final optimized cell is presented in Table 1. Using the developed modeling tool, charging and discharging cycles can be simulated in approximately 2 min,

Table 1. Overview of the Optimized Cell Parameters

positive electrode	nickel hydroxide
positive electrode thickness	3 mm
negative electrode	iron hydroxide
negative electrode thickness	2.25 mm
electrolyte	5 M KOH
electrode void fraction	0.35
battery capacity	3.5 Ah
hydrogen production	0.03 mol
energy efficiency	86%
pressure	Ambient
temperature	Ambient

reducing the time required to optimize for specific parameters. This facilitates the iterative design process and allows for many quick modifications in the unit cell layout.

4. CONCLUSIONS

We have developed a COMSOL Multiphysics model for the optimization of the battolyser, an integrated battery, and electrolyzer system. The model includes the electrochemical reactions related to battery charging and discharging, electrochemical reactions of hydrogen and oxygen production, transport mechanisms through the electrolyte gap, membrane and porous electrodes, and effective diffusivity and conductivity inside the porous electrodes. We validated the model with experimental results. Using the simulation results, we showed that the optimum electrode thickness is smaller than that of the commercial Ni−Fe battery electrodes used, 0.75 times the commercial electrode thickness, corresponding to an electrode thickness of 3 mm for the nickel electrode and 2.25 mm for the iron electrode. Optimizing for the porosity of the electrodes, we found that the optimum range of electrode void fraction lies between 0.15 and 0.35. Both modifications result in a combined overall efficiency of 86%, compared to a base-case efficiency of 80%.

The electronic resistance from the electrode material and battery capacity are the main limitations of the battolyser design. Battery electrodes are comparatively orders of magnitude thicker than those used in alkaline electrolysis. Therefore, the optimization of the integrated device is a complex process with many trade-offs and depends on application demands. Depending on the application profile of the device and the main product required—being hydrogen or electricity—the system can easily be optimized by running these simulations.

For a combined approach where both battery storage and hydrogen production are used, an optimized cell design was obtained by modifying the electrode thickness and porosity. Electrolyte conductivity and gap width were also optimized. However, because of the high ionic conductivity of the electrolyte and limited current density, the effect is negligible.

■ ASSOCIATED CONTENT

Supporting Information

The Supporting Information is available free of charge at https://pubs.acs.org/doi/10.1021/acs.iecr.1c00990.

> Model parameters and time-dependent equations, experimental details of the materials used, including elemental composition, SEM, X-ray diffraction, and BET surface area calculation, experimental details for the validation and further modeling results including different charging rates, gap thickness variations and electrolyte conductivity modifications, and further simulation results of the electrolyte concentration profiles (PDF)

■ AUTHOR INFORMATION

Corresponding Author

Ruud Kortlever − *Large-Scale Energy Storage Section, Department of Process & Energy, Faculty of Mechanical, Maritime and Materials Engineering, Delft University of Technology, 2628 CB Delft, The Netherlands;* orcid.org/0000-0001-9412-7480; Email: r.kortlever@tudelft.nl

Authors

Andrea Mangel Raventos − *Large-Scale Energy Storage Section, Department of Process & Energy, Faculty of Mechanical, Maritime and Materials Engineering, Delft University of Technology, 2628 CB Delft, The Netherlands*

Gerard Kluivers − *Large-Scale Energy Storage Section, Department of Process & Energy, Faculty of Mechanical, Maritime and Materials Engineering, Delft University of Technology, 2628 CB Delft, The Netherlands*

J.W. Haverkort − *Energy Technology Section, Department of Process & Energy, Faculty of Mechanical, Maritime and Materials Engineering, Delft University of Technology, 2628 CB Delft, The Netherlands*

Wiebren de Jong − *Large-Scale Energy Storage Section, Department of Process & Energy, Faculty of Mechanical, Maritime and Materials Engineering, Delft University of Technology, 2628 CB Delft, The Netherlands*

Fokko M. Mulder − *Materials for Energy Conversion and Storage, Department of Chemical Engineering, Faculty of Applied Science, Delft University of Technology, 2629 HZ Delft, The Netherlands;* orcid.org/0000-0003-0526-7081

Complete contact information is available at: https://pubs.acs.org/10.1021/acs.iecr.1c00990

Notes

The authors declare no competing financial interest.

■ REFERENCES

(1) Denholm, P.; Ela, E.; Kirby, B.; Milligan, M. *The Role of Energy Storage with Renewable Electricity Generation*; 2010.

(2) International Energy Agency. *World Energy Outlook 2020 − Analysis*, 2020.

(3) Ibrahim, H.; Ilinca, A.; Perron, J. Energy Storage Systems-Characteristics and Comparisons. *Renewable Sustainable Energy Rev.* **2008**, *12*, 1221−1250.

(4) Yekini Suberu, M.; Wazir Mustafa, M.; Bashir, N. Energy Storage Systems for Renewable Energy Power Sector Integration and Mitigation of Intermittency. *Renewable Sustainable Energy Rev.* **2014**, *35*, 499−514.

(5) Chu, S.; Majumdar, A. Opportunities and Challenges for a Sustainable Energy Future. *Nature* **2012**, *488*, 294−303.

(6) Mulder, F. M. Implications of Diurnal and Seasonal Variations in Renewable Energy Generation for Large Scale Energy Storage. *J. Renewable Sustainable Energy* **2014**, *6*, No. 033105.

(7) Evans, A.; Strezov, V.; Evans, T. J. Assessment of Utility Energy Storage Options for Increased Renewable Energy Penetration. *Renewable Sustainable Energy Rev.* **2012**, *16*, 4141−4147.

(8) Barton, J. P.; Gammon, R. J. L.; Rahil, A. Characterisation of a Nickel-Iron Battolyser, an Integrated Battery and Electrolyser. *Front. Energy Res.* **2020**, *8*, No. 509052.

(9) Agbossou, K.; Kolhe, M.; Hamelin, J.; Bose, T. K. Performance of a Stand-Alone Renewable Energy System Based on Energy Storage as Hydrogen. *IEEE Trans. Energy Convers.* **2004**, *19*, 633−640.

(10) Nair, N. K. C.; Garimella, N. Battery Energy Storage Systems: Assessment for Small-Scale Renewable Energy Integration. *Energy Build.* **2010**, *42*, 2124−2130.

(11) Quadrelli, R.; Peterson, S. The Energy-Climate Challenge: Recent Trends in CO2 Emissions from Fuel Combustion. *Energy Policy* **2007**, *35*, 5938−5952.

(12) Ramachandran, R.; Menon, R. K. An Overview of Industrial Uses of Hydrogen. *Int. J. Hydrogen Energy* **1998**, 593−598.

(13) Mulder, F. M.; Weninger, B. M. H. H.; Middelkoop, J.; Ooms, F. G. B. B.; Schreuders, H.; H Weninger, B. M.; Middelkoop, J.; B Ooms, F. G.; Schreuders, H. Efficient Electricity Storage with the Battolyser, an Integrated Ni-Fe Battery and Electrolyser. *Energy Environ. Sci.* **2016**, *10*, 756−764.

(14) Salkind, A. J. *Alkaline Storage Batteries*; Wiley: New York, 1969.

(15) Hariprakash, B.; Martha, S. K.; Hegde, M. S.; Shukla, A. K. A Sealed, Starved-Electrolyte Nickel-Iron Battery. *J. Appl. Electrochem.* **2005**, *35*, 27−32.

(16) Shukla, A. K.; Ravikumar, M. K.; Balasubramanian, T. S. Nickel/Iron Batteries. *J. Power Sources* **1994**, *51*, 29−36.

(17) Sandeep, K. C.; Kamath, S.; Mistry, K.; Kumar, M. A.; Bhattacharya, S. K.; Bhanja, K.; Mohan, S. Experimental Studies and Modeling of Advanced Alkaline Water Electrolyser with Porous Nickel Electrodes for Hydrogen Production. *Int. J. Hydrogen Energy* **2017**, *42*, 12094−12103.

(18) Ulleberg, Ø. Modeling of Advanced Alkaline Electrolyzers a System Simulation Approach. *Int. J. Hydrogen Energy* **2003**, *28*, 21−33.

(19) Rodríguez, J.; Amores, E. CFD Modeling and Experimental Validation of an Alkaline Water Electrolysis Cell for Hydrogen Production. *Processes* **2020**, *8*, 1−17.

(20) Lao-atiman, W.; Bumroongsil, K.; Arpornwichanop, A.; Bumroongsakulsawat, P.; Olaru, S.; Kheawhom, S. Model-Based Analysis of an Integrated Zinc-Air Flow Battery/Zinc Electrolyzer System. *Front. Energy Res.* **2019**, *7* () DOI: 10.3389/fenrg.2019.00015.

(21) Yao, S.; Zhou, R.; Huang, X.; Liu, D.; Cheng, J. Three-Dimensional Transient Model of Zinc-Nickel Single Flow Battery Considering Side Reactions. *Electrochim. Acta* **2021**, *374*, No. 137895.

(22) Paxton, B.; Polymers, M. B. A.; Newman, J. Modeling of Nickel/Metal Hydride Batteries. *J. Electrochem. Soc.* **1997**, *144*, 3818−3831.

(23) Vogt, H. Mechanisms of Mass Transfer of Dissolved Gas from a Gas-Evolving Electrode and Their Effect on Mass Transfer Coefficient and Concentration Overpotential. *J. Appl. Electrochem.* **1989**, *19*, 713−719.

(24) Burdyny, T.; Graham, P. J.; Pang, Y.; Dinh, C.; Liu, M.; Sargent, E. H.; Sinton, D. Nanomorphology-Enhanced Gas-Evolution Intensifies CO2 Reduction Electrochemistry. *ACS Sustainable Chem. Eng.* **2017**, *5*, 4031−4040.

(25) AGFA Specialty Products. ZIRFON PERL UTP 500 - Specialty Products, http://www.agfa.com/specialty-products/solutions/membranes/zirfon-perl-utp-500/ (accessed Mar 7, 2018).

(26) Kuang, Y.; Chen, C.; Kirsch, D.; Hu, L. Thick Electrode Batteries: Principles, Opportunities, and Challenges. *Adv. Energy Mater.* **2019**, *9*, 1−19.

(27) Elango, R.; Demortière, A.; De Andrade, V.; Morcrette, M.; Seznec, V. Thick Binder-Free Electrodes for Li−Ion Battery Fabricated Using Templating Approach and Spark Plasma Sintering Reveals High Areal Capacity. *Adv. Energy Mater.* **2018**, *8*, 1−8.

(28) Haverkort, J. W. A Theoretical Analysis of the Optimal Electrode Thickness and Porosity. *Electrochim. Acta* **2019**, *295*, 846−860.

(29) Gilliam, R. J.; Graydon, J. W.; Kirk, D. W.; Thorpe, S. J. A Review of Specific Conductivities of Potassium Hydroxide Solutions for Various Concentrations and Temperatures. *Int. J. Hydrogen Energy* **2007**, *32*, 359−364.